nature communications

Article

https://doi.org/10.1038/s41467-025-56797-8

Conserved GTPase OLA1 promotes efficient translation on D/E-rich mRNA

Received: 21 May 2024

Accepted: 30 January 2025

Published online: 11 February 2025

Check for updates

Ting Yu[1,2,4], Xin Li[1,2,4], Wanlin Dong[1,2], Qixin Zhou[1,2], Qingrong Li[1,2,3], Zisuo Du[1,2] & Fuxing Zeng[1,2]

The TRAFAC (translation factors) GTPase OLA1 plays a critical role in various stress responses and is implicated in the regulation of tumor progression. It is conserved from bacteria to eukaryotes and regulates the translation through binding to the ribosome. Here, we report the cryo-electron microscopy structure of its *Escherichia coli* homolog, YchF, with the 50S subunit. In this structure, YchF is positioned at the side of the 50S subunit by engaging with uL14, bL19, and rRNA helix H62 through its helical and ATPase domains. We further demonstrate that the helical domain is essential for OLA1/YchF to function. A comprehensive analysis of the structure and Ribo-seq data points out that OLA1/YchF promotes the splitting of ribosomes into subunits on D/E-rich mRNA. Our findings provide crucial structural insights into the molecular mechanism of OLA1/YchF-associated translation-stalling regulation, which maintains the translation of genes involved in stress response and tumor progression.

GTPases are essential regulatory proteins that are highly conserved across species. They play crucial roles in regulating various biological processes, including signal transduction, intercellular transport, protein synthesis, ribosome biogenesis, and so on[1–3]. Based on the phylogenetic and structural analyses, GTPases can be divided into two large superclasses: SIMIBI (Signal Recognition GTPases and the MinD and BioD) superclass and TRAFAC (Translation Factor) superclass[1]. OLA1 and its bacteria homolog YchF belong to the TRAFAC class, Obg (spo0B-associated GTP-binding protein) family, and YchF subfamily of P-loop GTPases[4,5]. The OLA1/YchF proteins possess a core ATPase domain, a C-terminal TGS domain, and an inserted helical domain (Supplementary Fig. 1) and are ubiquitously expressed in a majority of organisms, including bacteria, plants, and humans, sharing more than 40% sequence identity (Supplementary Fig. 2)[6]. The G4 motif ((N/T)KxD) in the YchF subfamily exhibits a unique (N/T)(M/L/V)xE amino acid sequence, leading to the members losing GTP specificity and preferentially hydrolyzing ATP rather than GTP[5,7].

OLA1/YchF is involved in various cellular stress response pathways, such as heat shock, integrated stress, cell adhesion, and antioxidant responses[8,9]. It is also implicated in the regulation of tumor progression in numerous types of cancer, including breast, lung, and hepatocellular cancer[10–12]. Accumulating reports show that OLA1 is highly expressed in most cancers and could be a potential biomarker and therapeutic target for cancer[10,13–15]. OLA1 also works as an intrinsic stress response regulator, including oxidative stress[6] and heat shock[16,17]. Heat shock protein 70 (HSP70) is a key molecule in different types of cancer, and high expression of HSP70 is associated with poor tumor progression[18]. OLA1 regulates HSP70 protein stability to inhibit shock-induced cell death[16]. OLA1 also interacts with BRCA1 and BRCA1-associated RING domain protein 1, which affects centrosome function and is suspected to lead to carcinogenesis in hereditary breast and ovarian cancer[11,19,20].

Growing evidence shows that OLA1/YchF plays important roles in translation regulation on a subset of mRNAs, such as leaderless mRNAs encoding stress response proteins essential for cell survival[21]. Human OLA1 has been implicated in translation initiation by interacting with eIF2, thereby preventing its binding to the initiator methionyl-tRNA[22]. Conversely, under stress conditions, the down-regulation of OLA1

[1]Department of Systems Biology, School of Life Sciences, Southern University of Science and Technology, Shenzhen, Guangdong, PR China. [2]Institute for Biological Electron Microscopy, Southern University of Science and Technology, Shenzhen, Guangdong, PR China. [3]Present address: Skaggs School of Pharmacy and Pharmaceutical Sciences, University of California, San Diego, CA, USA. [4]These authors contributed equally: Ting Yu, Xin Li.
e-mail: zengfx@sustech.edu.cn

enhances translation initiation and mitigate the integrated stress response (ISR)[22,23]. A recent study in *Mollicutes* found that YchF is one of the 104 core set proteins that sustain ribosome biogenesis and the translation of the genetic code in self-replicating bacteria with reduced genomes[24]. Ribosome binding of OLA1/YchF has been observed in *E.coli*[21,25–27], yeast[17], *Trypanosoma*[4], plants[7], and human cells[22]. The available data suggest that YchF/OLA1 binds not only to fully assembled ribosomes but also independently to the small and large ribosomal subunits. Moreover, the 70S ribosome has been reported to stimulate the ATPase activity of YchF[26]. Recent biochemical studies using UV-inducible crosslinkers locate YchF at the E-site on the 30S small ribosomal subunit[21]. Despite these advances, questions remain unanswered regarding the molecular details of ribosome binding and translation regulation, as well as the exact roles of OLA1/YchF during these processes. One major reason for this gap is the lack of structural data capturing OLA1/YchF in complex with ribosomes.

Here, we report that OLA1/YchF binds to the ribosomal large subunit and promotes efficient translation on D/E-rich mRNA. Disruption in translation can be caused by truncated mRNA or mRNA with specific structures/sequences[28]. Rescuing stalled ribosomes on these mRNAs requires numerous ribosome-associated proteins to release the nascent peptide and split the ribosome. For instance, the proteins Dom34, Hbs1 and Rli1 target ribosomes with truncated mRNA in eukaryotes, catalyzing the splitting of subunit[28]. Stalls on specific mRNA structures/sequences can be resolved under optimal conditions, i.e., synthesis of P-rich is made possible by EF-P (in bacteria, eIF5A in eukaryotes and archaea)[29]. Stalling on R/K-rich mRNA is promoted by Rbg1/Tma46 complex or targeted/split by the RQT complex if ribosome collision occurs[30,31]. The bacteria ATP-Binding Cassette family-F (ABCF) proteins, YheS, YbiT/YkpA, EttA and Uup/YfmR could cope with these problematic nascent peptide sequences within the exit tunnel[32,33]. The ATP hydrolysis-coupled structural rearrangement is critical for handling ribosome stalling caused by nascent peptides[32]. Currently, there is limited research on D/E-rich mRNA. Through structural analysis and Ribo-seq data, we speculate that OLA1/YchF enhances translation on D/E-rich mRNA, a notion validated by our constructed reporter. OLA1/YchF binds to the large subunit at the uL14/bL19 position via its helical domain, preventing the re-association of split ribosomes. These findings not only provide deeper insights into OLA1/YchF function but also contribute to a better understanding of translation regulation on D/E-rich mRNA.

Results

Characterization of the YchF ribosomal complex

To obtain the ribosomal complexes with the protein associated, the binding of YchF to the ribosome was first assessed by passing it through a sucrose cushion under various conditions (Supplementary Fig. 3a). The results show that the wild-type YchF exhibits weak binding to the ribosomes in the presence of GDPCP or AMPPNP but not the hydrolyzable nucleotide (Supplementary Fig. 3a, labeled triangles). Consistent with this, the mutant variant YchF(H114A), which lacks the ATP hydrolysis function[34], displays similar binding affinity to the 70S in the presence of ATP (Supplementary Fig. 3a, band 6). The low affinity observed might be attributed to the fact that the in vitro conditions are not optimal for the YchF binding to ribosomes. These results are consistent with Becker M. et al., who reported that the proportion of YchF binding to 70S is only about 30%[26]. Therefore, we adopted a strategy of directly purifying the complex from cells with YchF(H114A) expressed in the background of wild-type *ychF* gene depletion using affinity chromatography (Supplementary Fig. 3b). Ribosome binding of YchF(H114A) was confirmed by sucrose gradient analysis (Supplementary Fig. 3c), as well as observing the ribosomal proteins in the elution from Ni-NTA purification (Supplementary Fig. 3d).

Surprisingly, 90% of the particles in the cryo-electron microscopy (cryo-EM) images are classified as 50S with YchF(H114A) bound, and only 10% are identified as empty ribosomes corresponding to the 70S ribosome, suggesting transient/weak binding of YchF to 70S (Supplementary Fig. 4a–c). The structure of the 50S complex is resolved to an overall resolution of 2.37 Å, with density for stacking nucleotides as well as amino acid side chains clearly resolved (Supplementary Fig. 4d, e and Supplementary Table 1). Weak but distinct density is observed near uL14, bL19 and H62, which can be fitted for YchF(H114A) protein (Fig. 1). A strategy of focused classification with subtracted signal (FCwSS) using a mask around YchF(H114A), uL14, bL19 and H62/63 is applied (Supplementary Fig. 4c). Two local reconstructions are obtained with 2.54 Å and 3.36 Å resolution, respectively (Supplementary Fig. 4c–g and Supplementary Table 1). By aligning the rRNA in the two local reconstructions, the helical domain showed identical conformations, while the ATPase and TGS domain exhibit a small shift (<2 Å) (Supplementary Fig. 4h). This shift may result from flexibility in the positions of the Helical, ATPase, and TGS domains, as these domains are primarily connected by loops. Both reconstructions feature strong density for YchF(H114A), indicating that the weak density in the combined reconstruction is due to the movement of the protein rather than sub-stoichiometric occupancy. Because YchF(H114A) binds at the 50S periphery, the local resolution is lower than the average map resolution (4–7 Å), yet the density allows to model the secondary structure of YchF(H114A) (Supplementary Fig. 5). In the local map at 2.54 Å, the side chains of the interface between YchF(H114A) and uL14, bL19, and H62 are clearly identified (Supplementary Fig. 5d–g). In the 3.36 Å local map, the main chain of all YchF(H114A) domains can be determined (Supplementary Fig. 5g). These cryo-EM maps allow for unambiguous model building for the 50S and YchF(H114A).

YchF binds to uL14, bL19, and H62 of 50S mainly through the helical domain

In the 50S•YchF(H114A) structure, the complex formation is promoted by the interactions between the helical domain of YchF and the grooves between uL14 and bL19, as well as H62 of 50S subunit (Fig. 1). First, three lysine residues (K152, K156, K159) on the tip of the helical domain establish interactions with the backbone of H62 in the region of G1703-A1705, forming the binding site 1 (Fig. 2a and b). These three positively charged residues are conserved among species (Fig. 2g and Supplementary Table 2). Together with the conserved K149, these four residues form a positively charged tip on the α4-α5 coiled coil, enabling interaction with the negatively charged backbone of rRNA H62 (Supplementary Fig. 6a). This type of interaction is common in RNA-binding proteins, such as the transcription elongation factor GreB, which could interact with RNA products through its positively charged coiled coil as well (Supplementary Fig. 6b)[35].

Secondly, the electrostatic potential distribution reflects a positively charged surface for uL14 and bL19, while a negatively charged surface is observed in the α4 and α5 helices of YchF, with the exception of the above-mentioned tip region (Supplementary Fig. 6c). This complementarity of the electrostatic potential generates electrostatic interactions between YchF and uL14, bL19 (Supplementary Fig. 6c). Among this region, polar interactions are also observed, as shown in binding site 2 and site 3 (Fig. 2c). In binding site 2, α5 of the helical domain docks into the groove of bL19 and consists of interactions between residues Q148, E166, N174 of YchF and K106, T104, I64 of bL19, respectively (Fig. 2d). In binding site 3, residues in the loops after α5 contribute additional polar interactions with uL14 and bL19 (Fig. 2e). The hydrophobic residue L181 of YchF might also provide hydrophobic interaction with F100 of uL14 (Fig. 2e). Moreover, residues in the tip after α7 of the ATPase domain offer further interactions for the binding of YchF (Fig. 2f).

In summary, YchF binds to rRNA H62 and ribosomal proteins uL14 and bL19 of the 50S subunit through its helical domain and ATPase domain via polar interactions. By analyzing the interface using the 'Protein interfaces, surfaces and assemblies' (PISA) service

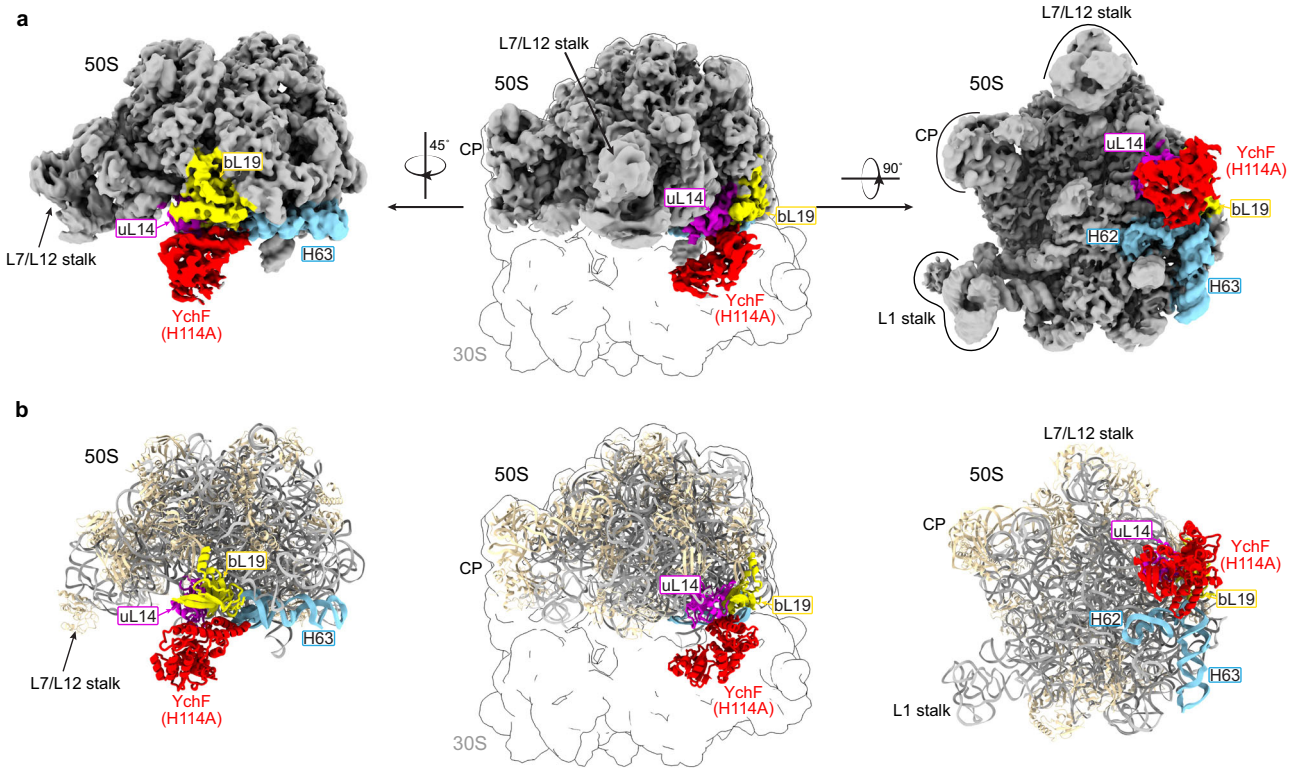

Fig. 1 | The overall structure of 50S•YchF complex. a Cryo-EM map of the YchF(H114A) in complex with 50S ribosomal subunit shown in three representative views. **b** Same as in (**a**) but shown with the cartoon model for the coordinates. The ribosome subunit, YchF(H114A), uL14, bL19, H62 and H63 are color-coded and labeled as indicated.

at the European Bioinformatics Institute[36], the area of these interfaces was calculated to be more than 643 Å^2. This accounts for a lower to modest interface among protein complexes[37,38], suggesting a weak or modest binding consistent with our experimental data discussed below.

YchF has the smallest cleft between helical and TGS domains on the ribosome

For translation-related GTPases or ATPases, such as Rbg1, binding to the ribosome usually induces a conformational change in the protein[39]. Here, we present structural alignment for the YchF between the ribosome-free and ribosome-bound states (Fig. 3a and Supplementary Table 3). Since the structure of *E. coli* YchF has not yet been determined, we here used YchF from other species for the structural alignment due to the high conservation of YchF among organisms (Supplementary Fig. 2). The YchF protein from *H.influenzae* (PDB: 1JAL), a gram-negative bacteria, was first aligned. Comparative analysis shows that the individual domains are structurally similar, with the RMSD values for each domain being less than 1.8 Å (Supplementary Fig. 7a–c). Since the helical domain is the main binding site to the 50S (Fig. 2), we aligned the helical domain from different species. Our alignment results reveal dramatic shifts and rotations in ATPase and TGS domains (Supplementary Fig. 7d). For instance, shift in the α7 helix of the ATPase domain towards uL14 causes a steric clash with the uL14 protein (Fig. 3a). This shift of α7 is primarily due to conformation changes between the free state and the 50S-associated state of YchF (Supplementary Fig. 7d). To systematically investigate the difference in the overall states of these two proteins, we measured the rotation angles and translation distances of the ATPase core region and the TGS domain between the two structures (Supplementary Fig. 7e). The results show that the ATPase domain shifts about 3.4 Å and rotates by 8.5°, while the TGS domain has a shift of 10.5 Å and a rotation of 22.3° (Supplementary Fig. 7e). The movements of these domains change the angle of cleft formed by the helical and TGS domains from 48.6° to 41.9° (Supplementary Table 3). This cleft has been reported to have potential binding activity with DNA[40]. Changes in the angle of this cleft might alter its substrate-binding properties. Furthermore, structural alignment with OLA1/YchF from *S. pombe*, *T.thermophilus*, *H. sapiens*, *O. sativa* (Supplementary Table 3) demonstrates different shifts and rotations. Alignment results further suggest the smallest cleft angle for YchF on the ribosome, which shows a proper conformation of α7 for the binding of protein to the 50S. The differences in conformation could be due to the binding on the ribosome, or may reflect conformational variations of OLA1/YchF in different nucleotide states. However, it is challenging to determine the specific causes without obtaining distinct structures of YchF from *E.coli* in various states.

The helical domain of YchF is essential for its functional activity

As YchF binds to the 50S subunit mainly through the helical domain, we next examined the effect of its removal on functional activity. The results show that deletion of YchF does not cause a significant phenotype under normal growth conditions, as reported previously[21] (Supplementary Fig. 8). However, the presence of YchF has been reported to cause hypersensitivity to oxidative stress[21,25]. As depicted in Fig. 3b, c, the expression of wild-type YchF protein in Δ*ychF* background exhibits a larger zone of clearance surrounding the H_2O_2 discs compared to the one with an empty vector, indicating a hypersensitivity to oxidative stress. In contrast, deletion of the helical domain partially removes this hypersensitivity (Fig. 3b, c), indicating that the helical domain plays a critical function in YchF function. These results demonstrate that the helical domain is essential for YchF functionality, probably through its binding to the 50S ribosomal subunits. However, as YchF is a multifunctional protein, other mechanisms should not be excluded.

https://doi.org/10.1038/s41467-025-56797-8

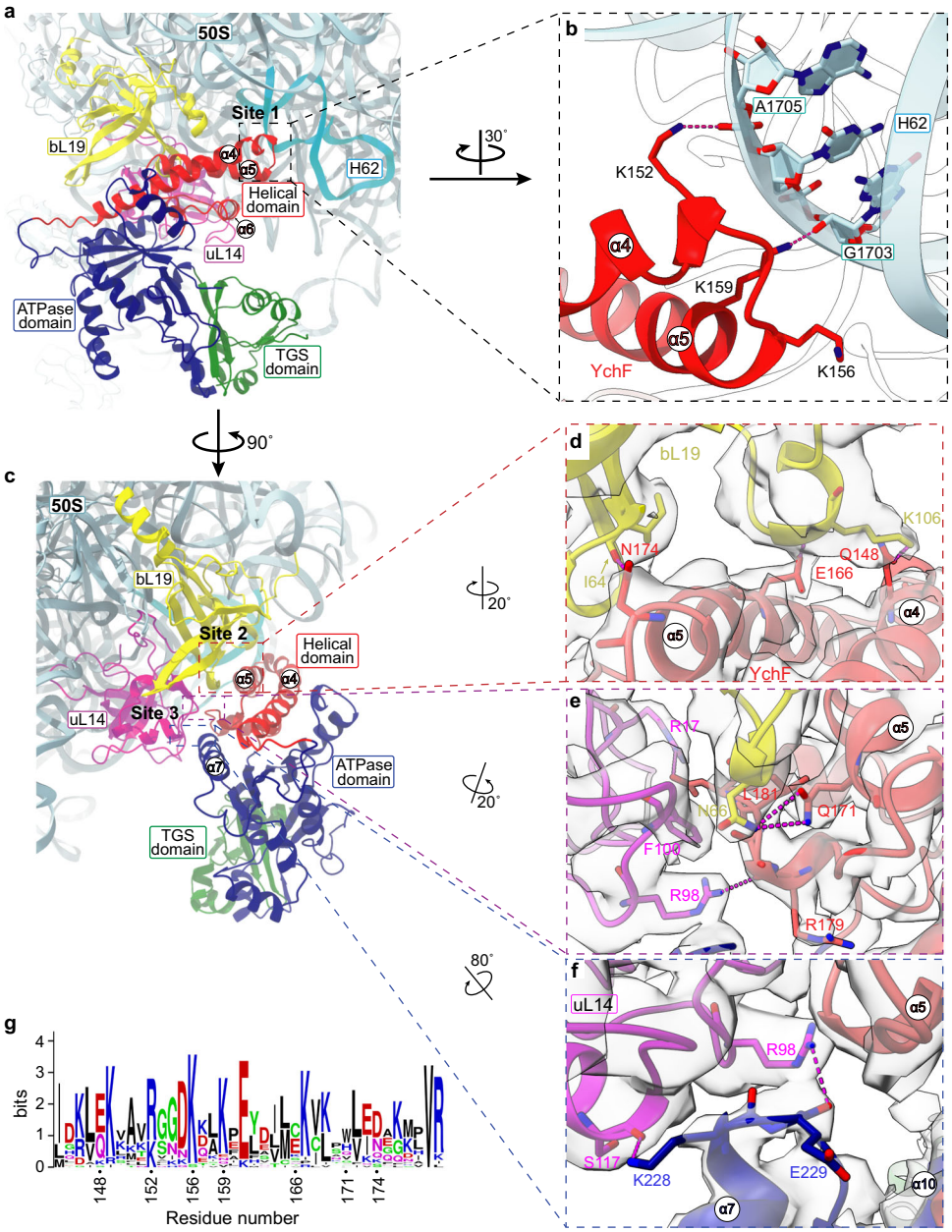

Fig. 2 | The detailed interactions between the YchF(H114A) and 50S subunit. **a**, **c** Overview of the interactions between YchF(H114A) (red/blue/green) and 50S (uL14: magenta; bL19: yellow; H62: cyan) shown in two representative views. **b** Magnified view of the region indicated by box in (**a**). The key residues of YchF and H62 involved in YchF-50S interactions are shown and labeled. **d**–**f**, Magnified views of the regions indicated by boxes in (**c**). The key residues of YchF and uL14, bL19 involved in YchF-50S interactions are shown and labeled. Cryo-EM map densities are shown in gray with the same level. **g** Sequence logos created in WebLogo shows that lysine and arginine are conserved in the tip of the helical domain among species. A total of 28 OLA1/YchF sequences from different species were used for the alignment (Supplementary Table 2).

YchF promotes the splitting of chloramphenicol-treated polysomes

The binding region of YchF on 50S is notable since it is one of the interfaces between the large and small subunits. In a mature 70S ribosome, uL14 and bL19 in the 50S interact with the rRNA helices h14 and h44 in the 30S, thus supporting the stability of the 70S ribosome[41]. RsfS is another protein that has been reported to bind to this region[42]. Different from YchF, RsfS interacts with uL14, bL19, and rRNA helix H95 (Supplementary Fig. 9a, b). Notably, the eukaryotic initiation factor 6 (eIF6) occupies the same binding site as RsfS[43] (Supplementary Fig. 9c). Both RsfS and eIF6 have been reported to possess ribosome anti-association activity, preventing the formation of 70S and 80S ribosomes, respectively[42,43]. We then set out to examine whether YchF could split ribosomes or prevent the formation of 70S. Incubation of purified YchF with 70S did show an increment of 30S and 50S peaks in the sucrose gradient experiments when 100-fold excess of YchF was used (Supplementary Fig. 9d, e). Lower amount (5-fold excess) of YchF did not increase the splitting of 70S. These results indicate that YchF binds weakly to the purified ribosomes or subunits, which is consistent with the binding assay shown in Supplementary Fig. 3a.

Considering that the YchF/50S complex was purified by pulldown, we turned to investigate the effects of YchF on ribosomes in cells. As shown in Fig. 3d, the addition of chloramphenicol to the Δ*ychF* cells stabilizes the polysome peaks in the sucrose gradient[44]. When YchF was added to the cell extracts, increased subunit peaks were observed in the presence of both ATP and AMPNP (Fig. 3e, f). In the absence of

https://doi.org/10.1038/s41467-025-56797-8

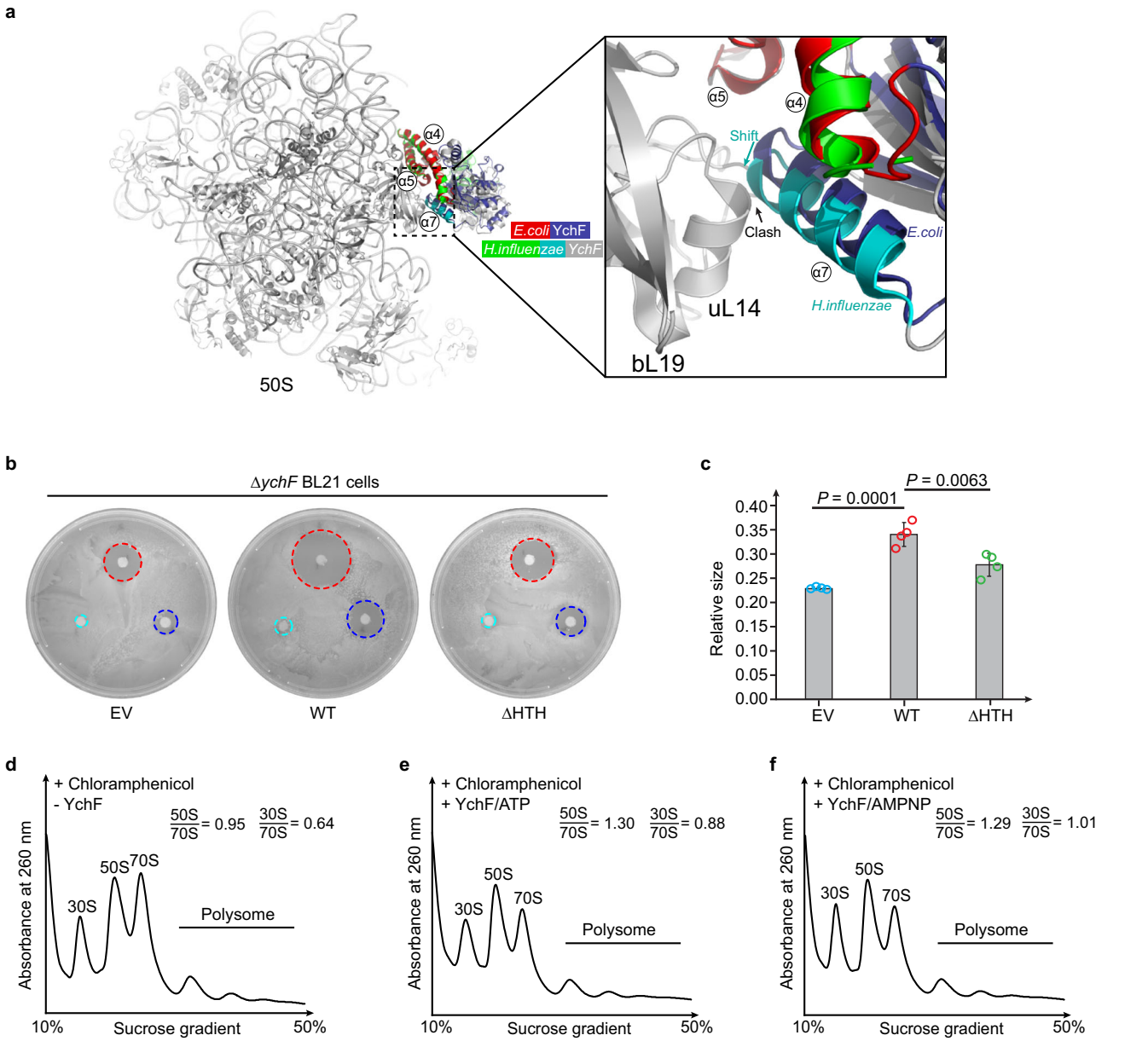

Fig. 3 | YchF promotes the dissociation of ribosomal subunits and the helical domain is required for its cellular function. a Alignment of helical domain (red) between YchF(H114A) obtained in this study and the crystal structure of *H.influenzae* YchF (PDB: 1JAL). Domains in the two proteins are color-coded and labeled as indicated. **b** Zones of *E. coli* growth inhibition by disc diffusion away from H_2O_2. 10 mM (cyan), 200 mM (blue) an 800 mM (red) of H_2O_2 were used for the plates expressing wild-type YchF (middle) and the one truncating helical domain (right). Empty vector was used as control (left). **c** Relative sizes of the red circles in (**b**) are quantified as the ratio of (diameter of red circle)/(diameter of plate). Data are presented as mean values ± SD. Experiments were performed in replicates ($n = 4$). *P* values were calculated by two-sided t-Test with unpaired two sample for means. EV, empty vector; WT, wild-type; ΔHTH, YchF with α4-α5 coiled coil truncated. Polysome profiling of *ΔychF* cells with the treatment of chloramphenicol in the absence (**d**) or presence of 5 μM YchF (**e**, **f**). 2 mM of ATP (**e**) and AMPNP (**f**) were added to the lysis buffer. Ratios of 50S and 70S peaks were calculated based on the peak heights. Source data are provided as a Source Data file.

YchF, the ratios of 30S and 50S to 70S were measured as 0.64 and 0.95, respectively. However, in the presence of YchF under ATP conditions, these ratios increased to 0.88 and 1.30, and under AMPPNP conditions, they increased to 1.01 and 1.29 (Fig. 3d–f). Both the 30S and 50S peaks showed an approximate 1.4- to 1.6-fold increase, suggesting that these increases are derived from the splitting of 70S ribosomes.

Based on the facts that YchF can also bind to 70S and its activity can be stimulated by the 70S ribosome[26], we speculated that under specific conditions, YchF could bind and promote the splitting of ribosome. After this process, YchF remains bound to the large subunit to prevent the reformation of the ribosome until the stress condition is eliminated. This suggests that the YchF/50S structure we obtained likely resembles the post-splitting complex, which may differ from the 70S encounter complex.

Deletion of OLA1 alters the translation of genes across diverse pathways

As described above, *E.coli* YchF possesses the ability to promote the splitting of ribosomes treated with chloramphenicol. To comprehensively investigate and compare ribosome dynamics in vivo at a genome-wide level, we utilized the ribosome profiling (Ribo-seq) method, which captures the ribosome-protected mRNA fragments[45]. Hela cells with the *OLA1* gene knocked out ($OLA1^{-/-}$) were used as the experimental group, while wild-type (WT) cells as the control.

https://doi.org/10.1038/s41467-025-56797-8

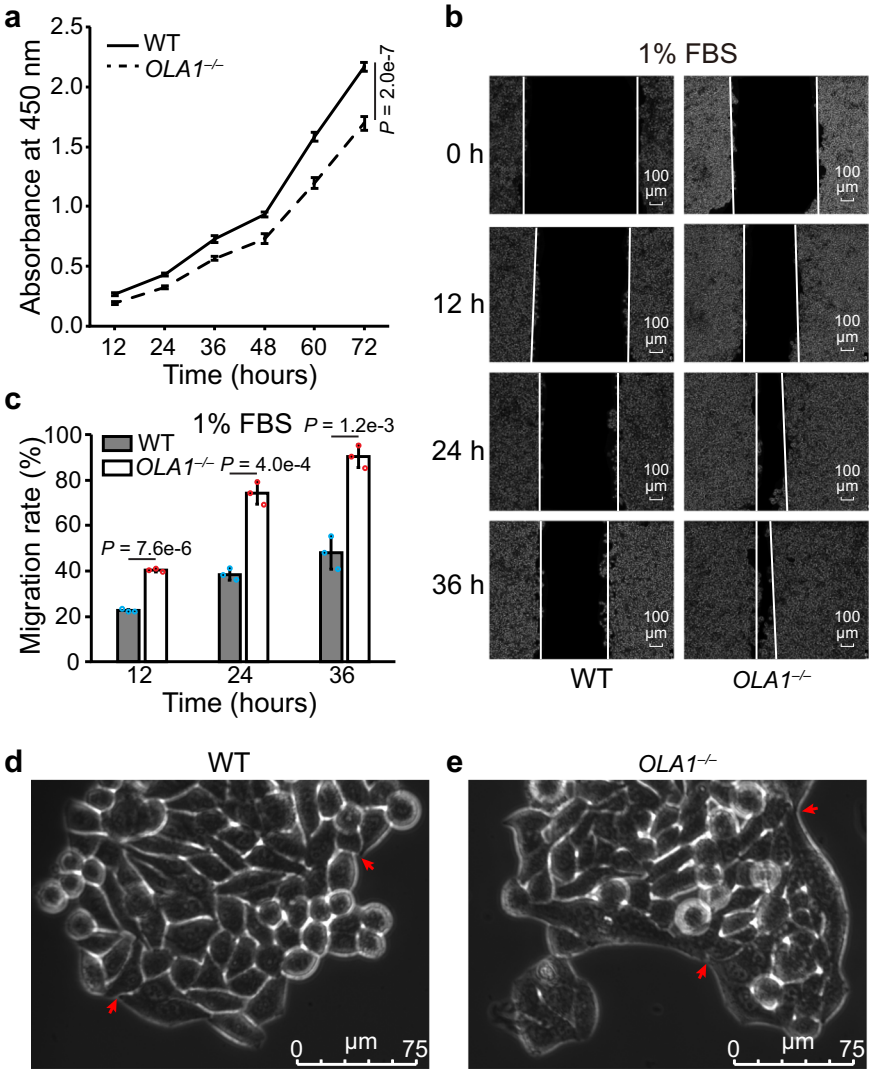

Fig. 4 | OLA1 plays critical cellular functions in Hela cells. a Cell viability detected by CCK8. Data are the average of five biological repeats and presented as mean ± SD. *P* value was calculated by two-sided Pearson correlation test. **b** Hela cells from WT (left panel) and *OLA1*$^{-/-}$ (right panel) were assayed for migration in a wound healing model with 1% FBS. Cell monolayers were scratched (bounded by white line) and the images were acquired at 0, 12, 24, and 36 h. **c** The wound closure area in (**b**) was quantified as the percentage of cells migrating into the wound with respect to the clear area at 0 h. The migration area was measured using ImageJ software. Data are the average of three biological repeats and presented as mean ± SD. *P* values were calculated by two-sided t-Test with unpaired two sample for means. Raw data points are shown in blue and red circles for WT and *OLA1*$^{-/-}$, respectively. Observation of cell morphology under a light microscope for wild-type (**d**) and *OLA1*$^{-/-}$ Hela cells (**e**). Representative cell boundaries are labeled with red arrows. Similar results were obtained for repeated experiments ($n = 5$). Source data are provided as a Source Data file.

Firstly, the phenotype of *OLA1*$^{-/-}$ cells was examined (Fig. 4). As shown in Fig. 4a, deletion of the *OLA1* gene moderately decreases the cell growth rate compared to wild-type cells. Interestingly, the wound-healing migration assay reveals that *OLA1*$^{-/-}$ cells migrate significantly faster than wild-type cells under conditions of 1–3% FBS (Fig. 4b, c and Supplementary Fig. 10). Furthermore, distinct boundaries are observed between the wild-type cells (Fig. 4d), whereas after deleting the *OLA1* gene, cells growing at the periphery exhibit a nearly fused state, with highly indistinct boundaries between cells (Fig. 4e). These observations suggest that, upon OLA1 deletion, alterations occur at the gene level associated with cell migration, resulting in enhanced migration rates of cells at the periphery.

Next, cells with 80% confluency were incubated with cycloheximide, a widely used translation inhibitor to arrest ribosomes on mRNA, and sent for RNA-seq and Ribo-seq analyses to characterize changes in mRNA abundance and translation efficiency (Supplementary Table 4). Three repeated experiments demonstrated good reproducibility, as the correlation coefficient was above 0.988 for mRNA-seq and above 0.920 for Ribo-seq data (Supplementary Fig. 11). The 3-nt periodicity patterns of both WT and *OLA1*$^{-/-}$ cells reveal distinct 0-frame features for reads of 25 and 28–30 nt, while 26 nt and 27 nt reads exhibit more pronounced −1 and +1 frame patterns, as depicted in Supplementary Fig. 12. After mapping to the genome, 2276 genes have the reads number exceeding 50, and they were used for further analysis in this study. RNA-seq data show that in *OLA1*$^{-/-}$ cells, 375 genes are up regulated at the mRNA level (Supplementary Fig. 13a), predominantly enriched in pathways such as blood vessel development and morphogenesis (Supplementary Fig. 13c). In contrast, mRNA levels of 679 genes are down regulated, and enriched in some immune response pathways (Supplementary Fig. 13d). Among these up regulated and down regulated genes, some are associated with cell migration, motility, and wounding (Supplementary Fig. 13c, d), which is consistent with the cell phenotype observed above (Fig. 4).

https://doi.org/10.1038/s41467-025-56797-8

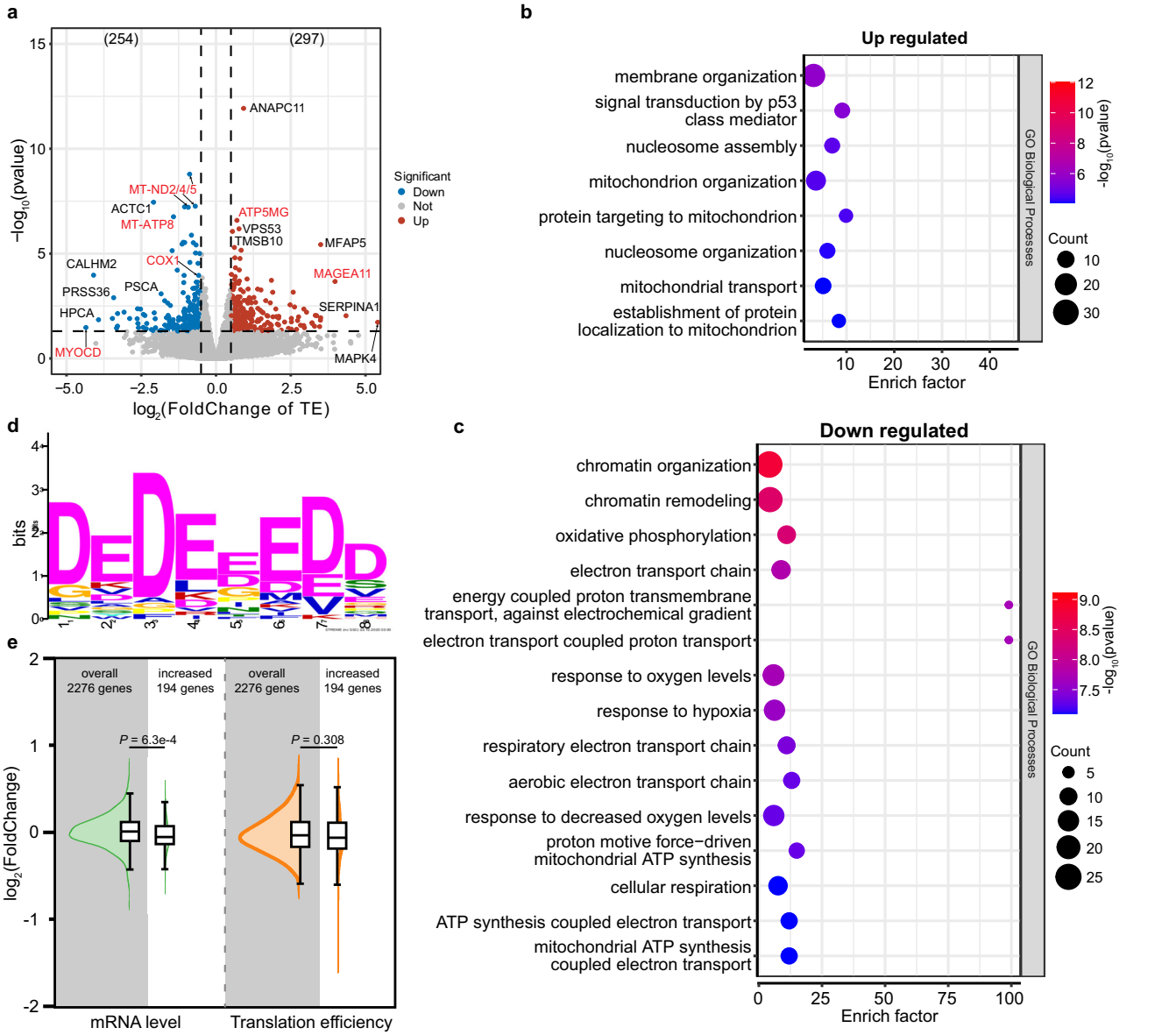

Fig. 5 | OLA1 regulates ribosome stalling on D/E-rich region. a Volcano plot showed the fold changes of translation efficiency. The numbers of regulated genes are shown in parentheses. A negative binomial statistical model with Wald test and Benjamini-Hochberg *P* value correction algorithm were used to identify different expressed genes. GO pathway enrichment analysis of the 297 up (**b**) and 254 down regulated (**c**) genes on translation level. Metascape utilizes the well-adopted hypergeometric test and Benjamini-Hochberg *P* value correction algorithm to identify all ontology terms as default setting in Metascape website **d** Sequence logo identified by MEME for the translation stalling. **e** Fold change of the mRNA and TE for all the 2276 analyzed genes and 194 genes with high ribosome stalling. Box indicates the 25 - 75% data, the bars represent 1.5IQR and the median is indicated as the line in the box. *P* values were calculated using the paired-sample Wilcoxon signed-rank test (two-sided). Source data are provided as a Source Data file.

At the translation level, we calculated the translational efficiency (TE) for each gene based on Ribo-seq data. Comparative analysis reveals that the TE of 297 genes is up regulated and associated with membrane and mitochondrial organization, such as the ATP5MG and MAGEA11 genes (Fig. 5a, b). Conversely, the TE of 254 genes is down regulated and enriched in pathways such as chromatin organization, electron transport, and response to hypoxia, including genes like COX1/2, MT-ATP8, and MYOCD (Fig. 5a, c). These changes are consistent with the previously reported response of *OLA1*$^{-/-}$ cells to H_2O_2 and mitochondrial electron transport[6,46]. Additionally, we observed that mRNA levels remain the same for most of the TE-changed genes, suggesting that the primary regulation occurs in the translation process.

OLA1 alleviates ribosome stalling at specific amino acids

Seemingly stochastic, yet pervasive ribosome stalls were observed at the individual gene level in our Ribo-seq data. We thus calculated the stalling score for each codon as described[30], with a focus on the ±10 amino acids regions. D/E-rich sequences stood out as one common feature for the ribosome stalling site in *OLA1*$^{-/-}$ cells (Fig. 5d). This result correlates well with the strong stalling effects of these two amino acids in ribosomes[47,48]. Since OLA1/YchF promotes the dissociation of a subset of ribosomes, we believe that the changes of translation stalling on the D/E-rich regions directly result from the regulation of OLA1.

From the 325 stalling-increased sites, we identified 194 genes. Only a few genes overlapped with the up or down-regulated genes at the mRNA and TE levels (Supplementary Fig. 14a, b), suggesting that

https://doi.org/10.1038/s41467-025-56797-8

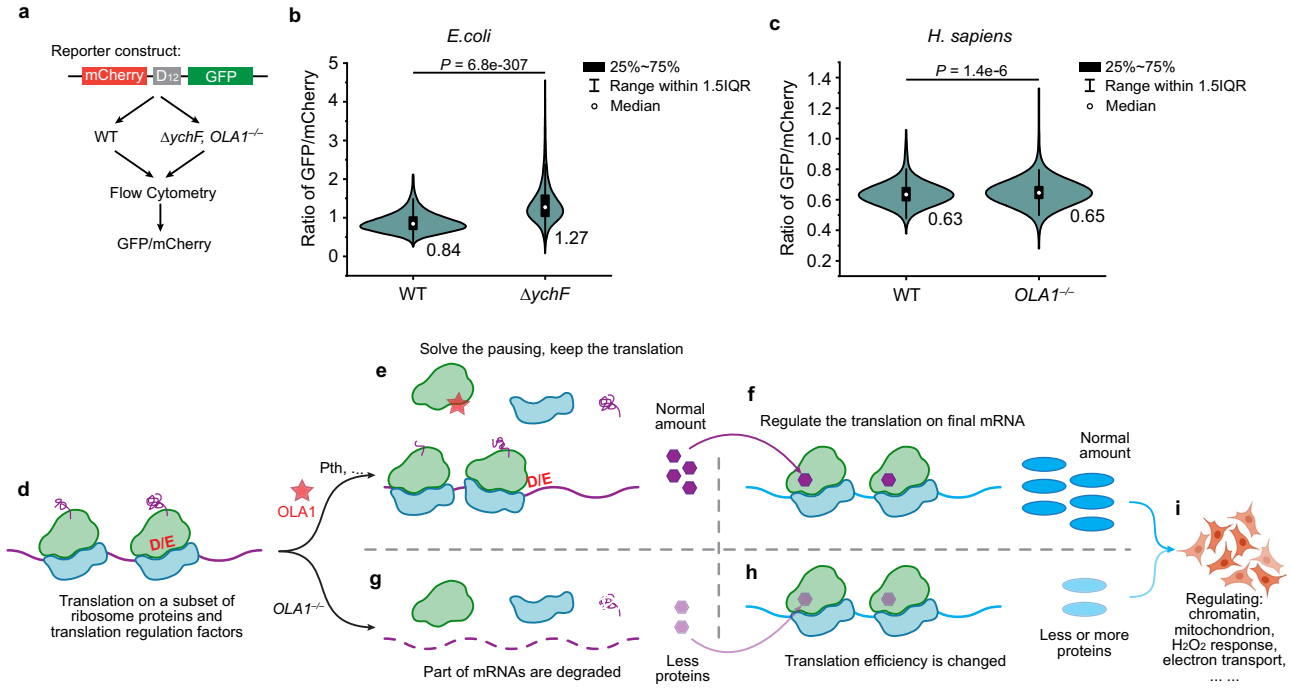

Fig. 6 | Model of the OLA1/YchF-mediated translation regulation. a Flowchart for validating the function of OLA1/YchF. D_{12}, twelve consecutive codons that encode Asp amino acids. **b**, **c** The violin plot displays the GFP/mCherry values in each cell. The experiment was conducted three times, and one of these repetitions is shown. The median values of the GFP/mCherry ratio are displayed in the figure, with *P* values calculated using the paired-sample Wilcoxon signed-rank test (two-sided). **d** Translation stalling happen on the mRNA for a subset of ribosome proteins and translation regulation factors. **e** OLA1/YchF and other proteins work together to solve the stalling on D/E-rich region and keep the translation at a normal level. **f** These translation-related proteins regulate the translation on the final mRNA. **g** Part of the mRNA with D/E-rich region are degraded when stalling can not be solved in the absence of OLA1/YchF. And the mRNA decay changes the amount of the translation-related proteins. **h** Less amount of the translation-related proteins generate heterogeneous ribosome complex, resulting in a change of translation efficiency on the final mRNA. **i** Final products further regulate various cell process. Source data are provided as a Source Data file.

these regulations were not a direct effect of OLA1 depletion. However, comparative analysis of all 2276 genes revealed a significant decrease in mRNA levels for these stalling-increased genes, while their TE remained unchanged, indicating that ribosome stalling may lead to increased degradation of mRNA in *OLA1*$^{-/-}$ cells (Fig. 5e). On the other hand, these stalling-increased genes were enriched in translation-related biological processes, including some translation factors and ribosomal proteins (Supplementary Fig. 14c). We thus hypothesized that OLA1 could alleviate ribosome stalling on D/E-rich regions of the translation-related genes by promoting the splitting of stalled ribosomes, ensuring sufficient proteins to regulate the translation of genes involved in H_2O_2 response, etc.

To verify the importance of OLA1/YchF on the translation of D/E-rich mRNA, we constructed an mCherry-D_{12}-GFP reporter system and measured the GFP/mCherry ratio in WT and Δ*ychF*/*OLA1*$^{-/-}$ cells (Fig. 6a–c). Results showed that deletion of *ychF* caused a significant increase in GFP/mCherry level, which can be interpreted as activation of the ribosome-associated quality control (RQC) pathway, leading to degradation of the mCherry protein. In *OLA1*$^{-/-}$ cells, an upward trend was also observed. However, the difference between WT and *OLA1*$^{-/-}$ cells was very small, and the spread overlapped, indicating the effect of OLA1 in human cells was not as conclusive as that of YchF in *E. coli* cells, possibly due to the more complex regulatory mechanisms in human cells.

The complex reported in our study likely represents the post splitting complex. How does OLA1/YchF recognize the stalled ribosome and promote the splitting? We noticed that the TGS domains of Rbg1 and RelA both could interact with h5 of the 18S/16S rRNA on the 80S/70S ribosome[30,49] (Supplementary Fig. 15). Structure-based alignment of the TGS domains in YchF, Rbg1 and RelA shows that their sequences are not conserved, but their structures are similar (Supplementary Fig. 15a). Rbg1 uses the loop after β3 and part of β4 to interact with h5 (Supplementary Fig. 15b). RelA adopts a similar pattern but including β3 for the interaction (Supplementary Fig. 15c). Superimposing of the TGS domain on the ribosome suggests that YchF may also be able to bind to this region. Since h5 is closed to uL14/bL19, which is the binding site of YchF on the 50S subunit, we hypothesize that OLA1/YchF might initially bind to the stalled ribosome via its TGS domain, possibly in conjunction with other ribosome-associated factors like peptidyl-tRNA hydrolase (Pth). Subsequently, through conformational changes, the large and small subunits may be split, with OLA1/YchF remaining on the large subunit to prevent re-association with the small subunit. This process resembles how, after the RQC trigger complex (RQT) separates the 60S from 40S, eIF6 binds to the 60S, preventing the formation of 80S[31].

Based on the results obtained in this study, we propose an OLA1/YchF-mediated translation regulation mechanism describing how OLA1/YchF affects cell growth by regulating translational arrest (Fig. 6d–f). In this model, we hypothesize that a subset of mRNAs encoding translation-related proteins, including ribosomal proteins and translation regulation factors, contains D/E-rich regions that could cause translation stalling (Fig. 6d). OLA1 and other regulatory proteins thus target these stalled ribosomes to promote their dissociation, ensuring the normal progress of translation (Fig. 6e). These translation-related proteins further regulate the translation of downstream proteins to support the normal growth of cells (Fig. 6f, i). However, in the absence of OLA1, some of the translation stalling leads to mRNA degradation, which reduces the production of these translation-related proteins (Figs. 5e and 6g). Heterogeneous ribosomes are then formed, which in turn alters the TE of downstream mRNAs (Figs. 5a and 6h). The net result is the changes in the levels of

downstream proteins, resulting in altered cellular responses to stress environments (Fig. 6i).

Discussion

Here we determined the cryo-EM structures of YchF bound to the 50S ribosomal subunit and investigated the functions of YchF on translation regulation. Our finding suggest that YchF binds to uL14, bL19, and H62 of the 50S subunit, located at the interface of the two ribosomal subunits. Given that two anti-association factors, RsfS and eIF6, bind to similar sites on the large subunits, we speculate that YchF performs a similar function to prevent the formation of functional ribosomes under certain stress conditions. Splitting assays demonstrated that YchF has the ability to promote the dissociation of large and small subunits of ribosomes treated with chloramphenicol. Deep analysis of the Ribo-seq data of *OLA1*$^{-/-}$ Hela cells also shows that the human homolog OLA1 could alleviate ribosome stalling at the D/E-rich region of mRNA. It is probable that OLA1/YchF promotes the splitting of these stalled ribosomes after the nascent peptides have been released.

Consistent with this idea, the gene *pth*, which codes Pth, has been reported to be co-expressed as a bicistronic mRNA with YchF[50]. Pth functions in tRNA recycling from stalled ribosomes[51]. In cases where the ribosomes stall with a short oligopeptide nascent chain, such as some mini-genes, upstream lead peptides, macrolide antibiotics, as well as certain patterns of codons soon after the start codon, the peptidyl-tRNA may dissociate from the ribosome without undergoing canonical translation termination[52]. Drop-off may be spontaneous or promoted by various translation factors, such as the ribosome recycling factor (RRF), elongation factor G (EF-G), and release factor 3 (RF3)[53–55]. We here speculate that in some cases, stalled ribosomes are possibly split by YchF via a mechanism not yet determined, followed by the release of peptidyl-tRNA for Pth. Similar to YchF, which is conserved across species, Pth is also present in bacterial and eukaryotic kingdoms but not archaea[52]. However, Pth-like activity has been detected in some archaea[56]. To fully unravel the mechanisms of splitting and anti-association for OLA1/YchF, further studies are needed to capture relevant intermediates on ribosomes.

Ribosome stalling is a common event in living cells, especially under stress conditions[57]. Ribosomes stall to allow co-translational protein folding, targeting or interactions, and this stalling is dictated by a combination of the mRNA sequence and structure, tRNA availability and the nascent peptide. However, ribosome stalling can also lead to ribosome collisions and co-translational degradation of both mRNA and nascent chain[58]. It has been reported that 63% of the conserved stall sites (CSS) could be explained by specific amino acids (Pro, Gly and Asp) at P-site, Glu at A-site, lysine stretches or negatively charged amino acids at the entrance to the exit tunnel[47]. As the entrance to the exit tunnel is narrow, it has been hypothesized that upon encountering it, the negative charge of amino acids might repel the negative charge of the exit tunnel and slow down the translation[47,59]. EF-P/eIF5A, Rbg1/Tma46, and some ABCF proteins have been reported to promote the translation on these stall sites[30,32,33]. Understanding how the translating ribosome tunes the different maturation steps that nascent proteins must undergo, what the timing of these maturation events is, and how degradation can be avoided when stalling is needed, is now possible by the emergence of methods to follow ribosome dynamics in vivo. Here, we showed that OLA1 is related to the ribosome stalling at the D/E-rich mRNA region. Alignment of the TGS domain between YchF, Rbg1 and RelA suggested a possible binding site of OLA1/YchF on the stalled ribosome, which is h5 of the small subunit rRNA. We still do not know the details of the splitting process due to the absence of structures of the pre-splitting complexes. However, based on the observation that YchF(H114A) binds to the 50S subunit, ATPase activity is most likely not required for ribosomal subunit dissociation, but important for YchF dissociation from the 50S subunit.

Through anti-association and splitting assays, we propose that OLA1/YchF may facilitate the dissociation of stalled ribosomes at D/E-rich regions through specific mechanisms, thereby ensuring efficient translation of D/E-rich mRNA. Since many ribosomal proteins contain D/E-rich sequences, the absence of OLA1/YchF could lead to the formation of heterogeneous ribosomes, ultimately resulting in aberrant expression of genes involved in processes such as membrane formation, chromatin organization, and hypoxia response. However, it is important to remember that OLA1/YchF is a multifunctional protein. In addition to binding the large ribosomal subunit, it can regulate translation through other mechanisms[21,22,60,61] and influence cell growth by interacting with proteins like HSP70[2,16,62,63]. Therefore, when studying the effects of YchF/OLA1 on cellular function, a comprehensive approach considering multiple perspectives is essential.

In summary, this study provides a key snapshot of how the universal conserved TRAFAC GTPase YchF binds to the ribosome and regulates the translation of D/E-rich mRNA. It also lays a solid foundation for future directions to unravel the mechanism that couples YchF with cancer cell growth.

Methods

Cells and strains

The Δ*ychF* BL21(DE3) *E. coli* strain and *OLA1*$^{-/-}$ Hela cell line were constructed using the CRISPR-U™-mediated genome engineering technique by RiboNext Biotechnology Co., LTD (Ningbo, China).

Multiple sequence alignment

The protein sequences of OLA1/YchF from *E. coli*, *H. influenzae*, *T. thermophilus*, *O. sativa*, *H. sapiens*, *M. musculus*, *D. rerio*, *C. elegans* and *S. cerevisiae* were obtained from UniProt (https://www.uniprot.org), and the sequence alignment was performed using multAlin (http://multalin.toulouse.inra.fr/multalin/). The alphaFold structure of *E. coli* YchF (AF-P0ABU2-F1) was used to obtain the information of secondary structure.

To generate the sequence logos, all the 28 reviewed items tagged as OLA1 or YchF in UniProt were downloaded, and the sequences of helical domains were extracted based on their multiple sequence alignment (Supplementary Table 2). Sequence logos were then generated using WebLogo (https://weblogo.berkeley.edu/logo.cgi) with the extracted sequences.

Preparation of *E. coli* ribosomes and YchF protein

70S ribosomes from the *E. coli* MRE600 strain were prepared as previously described[39]. The gene encoding *E. coli* YchF was cloned into the pET-28a vector, which carries an N-terminal 6×His tag. The H114A mutant was introduced using site-directed mutagenesis. To obtain the proteins, YchF or YchF(H114A) was expressed in an *E. coli* BL21 (DE3) strain at 16 °C overnight with 3 mM IPTG. YchF-ΔTGS was expressed in Rosetta (DE3) strain under the same conditions. Cells were harvested and lysed in buffer A (50 mM Tris-HCl, pH 7.5, 300 mM NaCl, 5% glycerol) using a French press. After removing cell debris by centrifugation at 20,000 × *g* for 40 min at 4 °C, the supernatant was loaded into a HisTrap HP column (Cytiva, Catalog No. 17524802). The proteins were eluted using an imidazole gradient.

Ribosome binding assay

To test the binding of YchF or YchF(H114A) to the ribosome, 10 μM of protein was incubated with 1 μM 70S ribosome for 30 min at 37 °C in a buffer B (20 mM HEPES-NaOH, pH 7.4, 50 mM NH_4Cl, 5 mM $MgCl_2$). Additional GDPCP, AMPPNP, or ATP was added to a final concentration of 2 mM when required. The reactions were then layered onto a 500 μL

1.1 M sucrose cushion in buffer B. Ribosomal complexes were pelleted through ultracentrifugation using a TLA-120.2 rotor at 354,406 × *g*, 4 °C for 15 min. Pellets were resuspended in 20 μL of buffer B and analyzed by western blot using anti-His antibody (abcam, Catalog No. ab18184).

Electron microscopy, data collection, and image processing

To enrich YchF-bound ribosomes, N-terminal 6×His-tagged YchF(H114A) was expressed in an *E.coli* BL21(DE3) strain with the *ychF* gene depleted (Δ*ychF*). Cells were grown to an OD_{600} of 0.8, and protein overexpression was induced with 0.3 mM IPTG at 16 °C for 10 h. Cells were harvested, resuspended in buffer B, and lysed using French press. Cell extracts were clarified by centrifugation at 20,000 × *g* for 40 min at 4 °C and passed through a Ni-NTA column. After washing three times with buffer B containing 30 mM imidazole, YchF(H114A)-bound complexes were eluted using 2 mL of buffer B with 100 mM imidazole. To remove excess free YchF, the eluted sample was layered onto a 300 μL 1.1 M sucrose cushion in buffer B and subjected to ultracentrifugation in a TLA-120.2 rotor at 354,406 × *g* for 15 min at 4 °C. The supernatant was carefully discarded, and the pellet was resuspended in 20 μL of buffer B. The complexes were crosslinked with 0.05% glutaraldehyde (Sangon Biotech, Catalog No. A600875-0100) for 30 min on ice. Crosslinking reactions were then quenched with 25 mM Tris-HCl (pH 7.5), and 0.01% n-do-decyl-D-maltoside (DDM, Sigma, Catalog No. D4641) was added to the final solution.

For sample preparation, 3 μL aliquots of ribosomal complexes at a concentration of 150 nM were incubated for 30 seconds on glow-discharged holey carbon grids with a thin-layer carbon film (Quantifoil, Catalog No. Q3100CR1.3). Grids were blotted using Vitrobot Mark IV (FEI) for 3 s with a blot force of 5 in 100% humidity at 4 °C, then were plunged frozen into liquid ethane. Data were collected in vitreous ice using Titan Krios G3i (D3796) transmission electron microscopes operating at 300 keV with FEI Falcon III detectors. A total of 3301 movies with 30 frames were acquired using a dose of 30 $e^{-}Å^{-2}$. The drifts of movie frames were corrected using MotionCor2[64], and the contrast transfer functions were determined using CTFFIND4[65].

Data processing was carried out in Relion 3.1[66]. A total of 939,306 particles were picked using Laplacian-of-Gaussian blob detection with diameters from 200 to 300 Å, and extracted for three rounds of reference-free 2D classification. A subset of 153,455 particles were selected and subjected to 3D classification. The classes displaying YchF density (137,631 particles) were selected for ctf-refine and polishing to yield a reconstruction with a resolution of 2.37 Å (global map). To increase the local resolution of YchF, a focused classification with subtracted signal (FCwSS) strategy was applied with the mask around the region of YchF, uL14, bL19, and H62/63. A 3D classification without alignment generated two focused reconstructions (local map #1 and #2) with resolutions of 2.54 Å and 3.36 Å, respectively. Resolutions were reported based upon the gold-standard Fourier shell correlation (FSC) of 0.143 criterion[66]. Local resolution was calculated by ResMol[67].

Model building, refinement, and validation

The large subunit of the high-resolution cryo-EM structure of *E. coli* 70S ribosome (PDB: 7K00)[68] was extracted and fit into the density map using rigid body fitting in Chimera[69]. The L9 protein, L1-stalk, and L7/L12-stalk of the 60S were fit separately using Coot[70]. The ribosome-bound YchF was built into the density map in coot using the model AF-P0ABU2-F1 calculated by alphaFold[71]. The model obtained was then refined using Phenix with secondary structure, RNA base-pair, sugar pucker and base stacking restrains[72]. The final model was validated using MolProbity[73]. Refinement statistics for the structure were summarized in Supplementary Table 1. Figures were made in ChimeraX[74] and Pymol.

Hydrogen peroxide disc diffusion assay

The hydrogen peroxide (H_2O_2) sensitivity assay was conducted using an H_2O_2 disc diffusion assay. Briefly, overnight cultures of tested strains were seeded into autoclaved LB medium and grew to a final OD_{600} of 0.5. An aliquot of 100 μL cells was then taken and evenly spread in petri discs. Circular sterile filter papers were soaked in 10 mM, 200 mM, and 800 mM of H_2O_2 solution and placed on top of the bacterial agar plates. The treated plates were incubated at 37 °C for 18 h, and clear zones reflecting the sensitivity of the bacterial strains to H_2O_2 were photographed and measured.

Ribosome splitting assay

For splitting on purified ribosomes, 0.3 μM 70S were incubated with 100-fold excess of YchF and 3.3 mM ATP on ice for 30 min. Reactions were then layered onto a 10-50% (w/v) sucrose gradient in buffer C (20 mM HEPES-NaOH, pH 7.4, 50 mM NH_4Cl, 3 mM $Mg(OAc)_2$) and further centrifuged in SW 40Ti rotor with 182,023 × *g*, 4 °C for 3.5 h. Purified 70S without incubating with YchF was used as control. Peaks of ribosomes were collected and monitored at 260 nm.

For splitting on the stalled ribosomes, the Δ*ychF* cells were first grown to OD_{600} of 0.6 and treated with 200 μg/mL chloramphenicol for 2 min. Cells were quickly harvested by centrifugation and resuspended in buffer B, followed by lysed in high-throughput tissue homogenizer with 65 Hz, 30 s twice. After removing cell debris by centrifugation at 20,000 × *g* for 20 min at 4 °C, the supernatant was incubated with 5 μM YchF or YchF-ΔTGS and 2 mM ATP or AMPPNP on ice for 30 min. Reactions were then layered onto a 10–50% (w/v) sucrose gradient in buffer B and further centrifuged in SW 40Ti rotor with 182,023 × *g*, 4 °C for 5 h. Peaks of ribosomes were collected and monitored at 260 nm.

Cell morphology observation

WT Hela and *OLA1*$^{-/-}$ cells were first cultured in DMEM medium with 10% FBS in 24 mm cell slides. After 24 h culture, the cells were washed twice with 1× PBS, and the cell slides were fixed with 4% paraformaldehyde solution at room temperature for 15 min. Slides were washed twice again with 1× PBS and made into temporary pack pieces. The cell pictures were captured by Nikon Ti-U in 20×.

CCK-8 assay

We used a CCK-8 kit (SparkJade, Catalog No. CT0001) to measure the proliferation of WT and *OLA1*$^{-/-}$ cells. A total of 5000 cells in a volume of 100 μL per well were cultured in five replicate wells in a 96-well plate with DMEM medium containing 10% FBS. Then, 10 μL of CCK-8 reagent was added to 90 μL to DMEM to generate a working solution, and the mixture was added to the well for 1 h incubation. The absorbance of the final solution was measured at 450 nm using a microplate reader.

Wound healing assay

Cells were cultured in a 6-well plate at a density of 2×10^6 cells for each well with 2 mL complete medium. After 12 h, when cells were confluent or nearly 98% confluent, a straight line was scratched with a sterile pipette tip, and the cells originally in the area of the line were removed by PBS. The rest cells were then cultured in different concentrations of FBS. Cell migration in the wound area was digitally photographed by phase contrast microscopy at 0–36 h. Wound healing was measured on the images and the migration area was calculated by Image J v2023.

RNA-Seq and Ribo-Seq

The WT and *OLA1*$^{-/-}$ Hela cells were first grown to 80% confluency in DMEM medium with 10% FBS. Cycloheximide was added to a final 100 μg/ml concentration and incubated for 10 min. Cells were then carefully scrapped off and sent to RiboNext Biotechnology Co., LTD (Ningbo, China) for library construction. Sequencing was performed

on the illumina novaseq 6000 platform for 50 M reads, yielding a total of six RNA-Seq and six Ribo-Seq datasets. Supplementary Table 4 provides a summary of the sequencing data sources.

Pre-processing of Raw Data and Analysis

The pre-processed data were categorized into WT and *OLA1*$^{-/-}$, corresponding to the experimental conditions. FastQC was employed to assess the quality of each file, ensuring their suitability for subsequent analyzes. Raw reads were then subjected to trimming using Cutadapt, applying specific parameters tailored to RNA-Seq (-a AGATCGGAAGAGCACACGTCTGAACTCCAGTCA -A AGATCGGAAGAGCGTCGTGTAGGGAAAGAGTGT -O 5) and Ribo-Seq samples (-a AACTGTAGGCACCATCAAT -O 5). Subsequently, clean reads were aligned against the *Homo sapiens* GRCh38 non-coding RNA (ncRNA) sequence set obtained from NCBI using Bowtie2[75]. Only unmapped non-ncRNA reads were retained for further analysis. Read mapping and counting against the *Homo sapiens* GRCh38[76] were conducted using HISAT2[77]. SAMtools[78] and the featurecounts. R program[79] were utilized to calculate read counts, Fragments Per Kilobase of transcript per Million mapped reads (FPKM), and Transcripts Per Kilobase of exon model per Million mapped reads (TPM) values within the open reading frame of encoding genes. These values were then used to quantify gene expression levels between WT and *OLA1*$^{-/-}$. Differential expression analysis was performed using the DESeq2 package[80] in RStudio, with significance determined by P values < 0.05 and $\log_2$FoldChange values >0.5 for up-regulated genes and <−0.5 for down-regulated genes. A volcano plot was generated using ggplot2. Translation efficiency (TE) was analyzed using Xtail software[81], with differentially expressed genes classified into up-regulated and down-regulated groups based on established criteria. Subsequently, GO functional enrichment analysis was conducted using the Metascape website (https://metascape.org) for both RNA-seq and TE differentially expressed genes. Quality control of Ribo-Seq bam data was performed using Ribotish[82], with periodicity analysis utilized to visualize frame bias and estimate P-site offsets for different read lengths.

Ribosome Stalling Analysis

Ribo-seq bam data were analyzed using RiboCounts[83], with the CDS sequence of *H. sapiens* GRCh38 serving as a reference. Ribo-Seq read counts for each gene were calculated, and the resulting values were averaged across three replicates for both WT and *OLA1*$^{-/-}$. Genes with fewer than 50 nucleotides were excluded to minimize noise, and the Stalling Score was calculated for the remaining 7987 genes as follows: Stalling Score = (Current Value/Total Values)* 100%. Here, Current Value represents the Ribo-Seq read counts values, while Total Values denote the summation values of Ribo-Seq read counts for 101 loci containing the top 50 and following 50 loci of the gene. If the stalling score of *OLA1*$^{-/-}$ sample is greater than twice the stalling score of the WT sample, it is considered to be the up-regulated stalling site. The 10 amino acid sequences before and after the stalling site were compared with no-different amino acid sequences to discover enriched motifs using the STREME module of MEME[84].

Flow cytometry

Cells (*E.coli* BL21 (DE3) or Hela) carrying the dual fluorescence reporter gene with a stalling sequence containing twelve consecutive Asp codons were grown to mid-log phase at 37 °C. Cells were then collected and about 10,000 cells were analyzed with a FACSCanto SORP flow cytometer for GFP and mCherry fluorescence detection using 488 and 561 nm excitation lasers, respectively. Data were analyzed by Flow Jo software. Cells with >10^3 RFU GFP and mCherry intensities were selected and the GFP/mCherry ratios were calculated and shown as violin plots. Flow cytometry was done in triplicate.

Reporting summary

Further information on research design is available in the Nature Portfolio Reporting Summary linked to this article.

Data availability

Electron microscopy maps have been deposited in the Electron Microscopy Data Bank as below:

EMD-37271 [https://www.ebi.ac.uk/emdb/EMD-37271] (The global map). EMD-37258 [https://www.ebi.ac.uk/emdb/EMD-37258] (The local maps #1). EMD-37263 [https://www.ebi.ac.uk/emdb/EMD-37263] (The local maps #2). Coordinates have been deposited in the Protein Data Bank as below: 8W51 [https://www.rcsb.org/structure/8W51] (The global model). 8KIE [https://www.rcsb.org/structure/8KIE] (The local model #1). The raw data of RNA-seq and Ribo-seq have been deposited in the SRA of NCBI as below: SRR25706713 [https://www.ncbi.nlm.nih.gov/sra/?term=SRR25706713+] (RNA-seq replicate #1 of *OLA1*$^{-/-}$ cells). SRR25706712 [https://www.ncbi.nlm.nih.gov/sra/?term=SRR25706712+] (RNA-seq replicate #2 of *OLA1*$^{-/-}$ cells). SRR25706711 [https://www.ncbi.nlm.nih.gov/sra/?term=SRR25706711+] (RNA-seq replicate #3 of *OLA1*$^{-/-}$ cells). SRR25706710 [https://www.ncbi.nlm.nih.gov/sra/?term=SRR25706710+] (RNA-seq replicate #1 of WT hela cells). SRR25706719 [https://www.ncbi.nlm.nih.gov/sra/?term=SRR25706719+] (RNA-seq replicate #2 of WT hela cells). SRR25706718 [https://www.ncbi.nlm.nih.gov/sra/?term=SRR25706718+] (RNA-seq replicate #3 of WT hela cells). SRR25706721 [https://www.ncbi.nlm.nih.gov/sra/?term=SRR25706721+] (Ribo-seq replicate #1 of *OLA1*$^{-/-}$ cells). SRR25706720 [https://www.ncbi.nlm.nih.gov/sra/?term=SRR25706720+] (Ribo-seq replicate #2 of *OLA1*$^{-/-}$ cells). SRR25706717 [https://www.ncbi.nlm.nih.gov/sra/?term=SRR25706717+] (Ribo-seq replicate #3 of *OLA1*$^{-/-}$ cells). SRR25706716 [https://www.ncbi.nlm.nih.gov/sra/?term=SRR25706716+] (Ribo-seq replicate #1 of WT hela cells). SRR25706715 [https://www.ncbi.nlm.nih.gov/sra/?term=SRR25706715+] (Ribo-seq replicate #2 of WT hela cells). SRR25706714 [https://www.ncbi.nlm.nih.gov/sra/?term=SRR25706714+] (Ribo-seq replicate #3 of WT hela cells). Source data are provided with this paper.

References

1. Leipe, D. D., Wolf, Y. I., Koonin, E. V. & Aravind, L. Classification and evolution of P-loop GTPases and related ATPases. *J. Mol. Biol.* **317**, 41–72 (2002).
2. Chen, T. et al. BARD1 is an ATPase activating protein for OLA1. *Biochim. Biophys. Acta Gen. Subj.* **1866**, 130099 (2022).
3. Landwehr, V., Milanov, M., Hong, J. & Koch, H. G. The role of the universally conserved ATPase YchF/Ola1 in translation regulation during cellular stress. *Microorganisms* **10**. https://doi.org/10.3390/microorganisms10010014 (2021).
4. Gradia, D. F. et al. Characterization of a novel Obg-like ATPase in the protozoan Trypanosoma cruzi. *Int J. Parasitol.* **39**, 49–58 (2009).
5. Koller-Eichhorn, R. et al. Human OLA1 defines an ATPase subfamily in the Obg family of GTP-binding proteins. *J. Biol. Chem.* **282**, 19928–19937 (2007).
6. Zhang, J., Rubio, V., Lieberman, M. W. & Shi, Z. Z. OLA1, an Obg-like ATPase, suppresses antioxidant response via nontranscriptional mechanisms. *Proc. Natl. Acad. Sci. USA* **106**, 15356–15361 (2009).
7. Cheung, M. Y. et al. ATP binding by the P-loop NTPase OsYchF1 (an unconventional G protein) contributes to biotic but not abiotic stress responses. *Proc. Natl. Acad. Sci. USA* **113**, 2648–2653 (2016).
8. Jeyabal, P. V., Rubio, V., Chen, H., Zhang, J. & Shi, Z. Z. Regulation of cell-matrix adhesion by OLA1, the Obg-like ATPase 1. *Biochem. Biophys. Res. Commun.* **444**, 568–574 (2014).
9. Schultz, A. et al. Decreased OLA1 (Obg-Like ATPase-1) expression drives ubiquitin-proteasome pathways to downregulate mitochondrial SOD2 (Superoxide Dismutase) in persistent pulmonary hypertension of the newborn. *Hypertension* **74**, 957–966 (2019).

10. Liu, J. et al. Obg-like ATPase 1 enhances chemoresistance of breast cancer via activation of TGF-β/Smad axis cascades. *Front. Pharm.* **11**, 666 (2020).
11. Yoshino, Y. et al. BRCA1-interacting protein OLA1 requires interaction with BARD1 to regulate centrosome number. *Mol. Cancer Res.* https://doi.org/10.1158/1541-7786.MCR-18-0269 (2018).
12. Sung, H. et al. Global cancer statistics 2020: GLOBOCAN estimates of incidence and mortality worldwide for 36 cancers in 185 countries. *CA Cancer J. Clin.* **71**, 209–249 (2021).
13. Dong, Y. et al. OLA1 is a potential prognostic molecular biomarker for endometrial cancer and promotes tumor progression. *Oncol. Lett.* **22**, 576 (2021).
14. Gomez, V. & Hergovich, A. OLA1 in centrosome biology alongside the BRCA1/BARD1 complex: looking beyond centrosomes. *Mol. Cell* **53**, 3–5 (2014).
15. Bian, R. et al. Knockdown of Obg-like ATPase 1 enhances sorafenib sensitivity by inhibition of GSK-3β/β-catenin signaling in hepatocellular carcinoma cells. *J. Gastrointest. Oncol.* **13**, 1255–1265 (2022).
16. Mao, R. F. et al. OLA1 protects cells in heat shock by stabilizing HSP70. *Cell Death Dis.* **4**, e491 (2013).
17. Dannenmaier, S. et al. Quantitative proteomics identifies the universally conserved ATPase Ola1p as a positive regulator of heat shock response in Saccharomyces cerevisiae. *J. Biol. Chem.* **297**, 101050 (2021).
18. Rosenzweig, R., Nillegoda, N. B., Mayer, M. P. & Bukau, B. The Hsp70 chaperone network. *Nat. Rev. Mol. Cell Biol.* **20**, 665–680 (2019).
19. Matsuzawa, A. et al. The BRCA1/BARD1-interacting protein OLA1 functions in centrosome regulation. *Mol. Cell* **53**, 101–114 (2014).
20. Takahashi, M. et al. OLA1 gene sequencing in patients with BRCA1/2 mutation-negative suspected hereditary breast and ovarian cancer. *Breast Cancer* **24**, 336–340 (2017).
21. Landwehr, V. et al. The universally conserved ATPase YchF regulates translation of leaderless mRNA in response to stress conditions. *Front. Mol Biosci.* **8**. https://doi.org/10.3389/fmolb.2021.643696 (2021).
22. Chen, H. et al. OLA1 regulates protein synthesis and integrated stress response by inhibiting eIF2 ternary complex formation. *Sci. Rep.* **5**, 13241 (2015).
23. Sun, H. et al. DOC45, a novel DNA damage-regulated nucleocytoplasmic ATPase that is overexpressed in multiple human malignancies. *Mol. Cancer Res.* **8**, 57–66 (2010).
24. Grosjean, H. et al. Predicting the minimal translation apparatus: lessons from the reductive evolution of mollicutes. *PLoS Genet.* **10**, e1004363 (2014).
25. Wenk, M. et al. A universally conserved ATPase regulates the oxidative stress response in Escherichia coli. *J. Biol. Chem.* **287**, 43585–43598 (2012).
26. Becker, M. et al. The 70S ribosome modulates the ATPase activity of Escherichia coli YchF. *RNA Biol.* **9**, 1288–1301 (2012).
27. Tomar, S. K., Kumar, P. & Prakash, B. Deciphering the catalytic machinery in a universally conserved ribosome binding ATPase YchF. *Biochem. Biophys. Res. Commun.* **408**, 459–464 (2011).
28. Buskirk, A. R. & Green, R. Ribosome pausing, arrest and rescue in bacteria and eukaryotes. *Philos. Trans. R. Soc. Lond. B Biol. Sci.* **372**. https://doi.org/10.1098/rstb.2016.0183 (2017).
29. Doerfel, L. K. et al. EF-P is essential for rapid synthesis of proteins containing consecutive proline residues. *Science* **339**, 85–88 (2013).
30. Zeng, F. et al. Conserved heterodimeric GTPase Rbg1/Tma46 promotes efficient translation in eukaryotic cells. *Cell Rep.* **37**, 109877 (2021).
31. Best, K. et al. Structural basis for clearing of ribosome collisions by the RQT complex. *Nat. Commun.* **14**, 921 (2023).
32. Chadani, Y. et al. The ABCF proteins in Escherichia coli individually cope with 'hard-to-translate' nascent peptide sequences. *Nucleic Acids Res.* **52**, 5825–5840 (2024).
33. Takada, H., Fujiwara, K., Atkinson, G. C., Chiba, S. & Hauryliuk, V. Resolution of ribosomal stalling by EF-P and ABCF ATPases YfmR and YkpA/YbiT. *Nucleic Acids Res.* **52**, 9854–9866 (2024).
34. Rosler, K. S., Mercier, E., Andrews, I. C. & Wieden, H. J. Histidine 114 Is Critical for ATP Hydrolysis by the Universally Conserved ATPase YchF. *J. Biol. Chem.* **290**, 18650–18661 (2015).
35. Abdelkareem, M. et al. Structural basis of transcription: RNA polymerase backtracking and its reactivation. *Mol. Cell* **75**, 298–309.e294 (2019).
36. Krissinel, E. & Henrick, K. Inference of macromolecular assemblies from crystalline state. *J. Mol. Biol.* **372**, 774–797 (2007).
37. Yang, Y. X., Wang, P. & Zhu, B. T. Importance of interface and surface areas in protein-protein binding affinity prediction: A machine learning analysis based on linear regression and artificial neural network. *Biophys.Chem.* **283**, 106762 (2022).
38. Chen, J., Sawyer, N. & Regan, L. Protein-protein interactions: general trends in the relationship between binding affinity and interfacial buried surface area. *Protein Sci.* **22**, 510–515 (2013).
39. Zeng, F. et al. Structural basis of co-translational quality control by ArfA and RF2 bound to ribosome. *Nature* **541**, 554–557 (2017).
40. Teplyakov, A. et al. Crystal structure of the YchF protein reveals binding sites for GTP and nucleic acid. *J. Bacteriol.* **185**, 4031–4037 (2003).
41. Noeske, J. et al. High-resolution structure of the Escherichia coli ribosome. *Nat. Struct. Mol. Biol.* **22**, 336–341 (2015).
42. Khusainov, I. et al. Mechanism of ribosome shutdown by RsfS in Staphylococcus aureus revealed by integrative structural biology approach. *Nat. Commun.* **11**, 1656 (2020).
43. Klinge, S., Voigts-Hoffmann, F., Leibundgut, M., Arpagaus, S. & Ban, N. Crystal structure of the eukaryotic 60S ribosomal subunit in complex with initiation factor 6. *Science* **334**, 941–948 (2011).
44. Kopik, N., Chrobak, O., Latoch, P., Kovalenko, M. & Starosta, A. L. RIBO-seq in bacteria: a sample collection and library preparation protocol for NGS sequencing. *J. Vis. Exp.* https://doi.org/10.3791/62544 (2021).
45. Ingolia, N. T., Brar, G. A., Rouskin, S., McGeachy, A. M. & Weissman, J. S. The ribosome profiling strategy for monitoring translation in vivo by deep sequencing of ribosome-protected mRNA fragments. *Nat. Protoc.* **7**, 1534–1550 (2012).
46. Kira, Y. & Nishikawa, M. The identification and characterization of a new GTP-binding protein (Gbp45) involved in cell proliferation and death related to mitochondrial function. *Cell. Mol. Biol. Lett.* **13**, 570–584 (2008).
47. Chyżyńska, K., Labun, K., Jones, C., Grellscheid, S. N. & Valen, E. Deep conservation of ribosome stall sites across RNA processing genes. *NAR Genom. Bioinform.* **3**, lqab038 (2021).
48. Sabi, R. & Tuller, T. A comparative genomics study on the effect of individual amino acids on ribosome stalling. *BMC Genom.* **16**, S5 (2015).
49. Loveland, A. B. et al. Ribosome*RelA structures reveal the mechanism of stringent response activation. *Elife* **5**. https://doi.org/10.7554/eLife.17029 (2016).
50. Cruz-Vera, L. R., Galindo, J. M. & Guarneros, G. Transcriptional analysis of the gene encoding peptidyl-tRNA hydrolase in Escherichia coli. *Microbiol. (Read.)* **148**, 3457–3466 (2002).
51. Muller, C., Crowe-McAuliffe, C. & Wilson, D. N. Ribosome rescue pathways in bacteria. *Front. Microbiol.* **12**, 652980 (2021).
52. Sharma, S. et al. Structural and functional insights into peptidyl-tRNA hydrolase. *Biochim. Biophys. Acta* **1844**, 1279–1288 (2014).
53. Vivanco-Domínguez, S. et al. Protein synthesis factors (RF1, RF2, RF3, RRF, and tmRNA) and peptidyl-tRNA hydrolase rescue stalled ribosomes at sense codons. *J. Mol. Biol.* **417**, 425–439 (2012).

54. Watanabe, Y., Nakamura, Y. & Ito, K. A novel class of bacterial translation factor RF3 mutations suggests specific structural domains for premature peptidyl-tRNA drop-off. *FEBS Lett.* **584**, 790–794 (2010).
55. Singh, N. S., Ahmad, R., Sangeetha, R. & Varshney, U. Recycling of ribosomal complexes stalled at the step of elongation in Escherichia coli. *J. Mol. Biol.* **380**, 451–464 (2008).
56. Fromant, M., Ferri-Fioni, M. L., Plateau, P. & Blanquet, S. Peptidyl-tRNA hydrolase from Sulfolobus solfataricus. *Nucleic Acids Res.* **31**, 3227–3235 (2003).
57. VanInsberghe, M., van den Berg, J., Andersson-Rolf, A., Clevers, H. & van Oudenaarden, A. Single-cell Ribo-seq reveals cell cycle-dependent translational pausing. *Nature* **597**, 561–565 (2021).
58. Collart, M. A. & Weiss, B. Ribosome pausing, a dangerous necessity for co-translational events. *Nucleic Acids Res.* **48**, 1043–1055 (2020).
59. Chiba, S. & Ito, K. Multisite ribosomal stalling: a unique mode of regulatory nascent chain action revealed for MifM. *Mol. Cell* **47**, 863–872 (2012).
60. Leiva, L. E. & Katz, A. Regulation of leaderless mRNA translation in bacteria. *Microorganisms* **10**. https://doi.org/10.3390/microorganisms10040723 (2022).
61. Leiva, L. E., Orellana, O., Ibba, M. & Katz, A. Enhanced translation of leaderless mRNAs under oxidative stress in Escherichia coli. *BioRxiv* https://doi.org/10.1101/2021.06.29.449897 (2021).
62. Fang, Z. et al. Aurora A polyubiquitinates the BRCA1-interacting protein OLA1 to promote centrosome maturation. *Cell Rep.* **42**, 112850 (2023).
63. Chang, C. W. et al. The BRCA1 BRCT promotes antisense RNA production and double-stranded RNA formation to suppress ribosomal R-loops. *Proc. Natl. Acad. Sci. USA* **119**, e2217542119 (2022).
64. Zheng, S. Q. et al. MotionCor2: anisotropic correction of beam-induced motion for improved cryo-electron microscopy. *Nat. Methods* **14**, 331–332 (2017).
65. Rohou, A. & Grigorieff, N. CTFFIND4: fast and accurate defocus estimation from electron micrographs. *J. Struct. Biol.* **192**, 216–221 (2015).
66. Zivanov, J. et al. New tools for automated high-resolution cryo-EM structure determination in RELION-3. *Elife* **7**. https://doi.org/10.7554/eLife.42166 (2018).
67. Kucukelbir, A., Sigworth, F. J. & Tagare, H. D. Quantifying the local resolution of cryo-EM density maps. *Nat. Methods* **11**, 63–65 (2014).
68. Watson, Z. L. et al. Structure of the bacterial ribosome at 2 A resolution. *Elife* **9**. https://doi.org/10.7554/eLife.60482 (2020).
69. Pettersen, E. F. et al. UCSF Chimera–a visualization system for exploratory research and analysis. *J. Comput. Chem.* **25**, 1605–1612 (2004).
70. Emsley, P., Lohkamp, B., Scott, W. G. & Cowtan, K. Features and development of Coot. *Acta Crystallogr. D Biol. Crystallogr.* **66**, 486–501 (2010).
71. Jumper, J. et al. Highly accurate protein structure prediction with AlphaFold. *Nature* **596**, 583–589 (2021).
72. Adams, P. D. et al. PHENIX: a comprehensive Python-based system for macromolecular structure solution. *Acta Crystallogr. D Biol. Crystallogr.* **66**, 213–221 (2010).
73. Chen, V. B. et al. MolProbity: all-atom structure validation for macromolecular crystallography. *Acta Crystallogr. D Biol. Crystallogr.* **66**, 12–21 (2010).
74. Pettersen, E. F. et al. UCSF ChimeraX: structure visualization for researchers, educators, and developers. *Protein Sci.* **30**, 70–82 (2021).
75. Langmead, B. & Salzberg, S. L. Fast gapped-read alignment with Bowtie 2. *Nat. Methods* **9**, 357–359 (2012).
76. Lander, E. S. et al. Initial sequencing and analysis of the human genome. *Nature* **409**, 860–921 (2001).
77. Kim, D., Paggi, J. M., Park, C., Bennett, C. & Salzberg, S. L. Graph-based genome alignment and genotyping with HISAT2 and HISAT-genotype. *Nat. Biotechnol.* **37**, 907–915 (2019).
78. Li, H. et al. The sequence alignment/map format and SAMtools. *Bioinformatics* **25**, 2078–2079 (2009).
79. Liao, Y., Smyth, G. K. & Shi, W. The R package Rsubread is easier, faster, cheaper and better for alignment and quantification of RNA sequencing reads. *Nucleic Acids Res.* **47**, e47 (2019).
80. Love, M. I., Huber, W. & Anders, S. Moderated estimation of fold change and dispersion for RNA-seq data with DESeq2. *Genome Biol.* **15**, 550 (2014).
81. Xiao, Z., Zou, Q., Liu, Y. & Yang, X. Genome-wide assessment of differential translations with ribosome profiling data. *Nat. Commun.* **7**, 11194 (2016).
82. Zhang, P. et al. Genome-wide identification and differential analysis of translational initiation. *Nat. Commun.* **8**, 1749 (2017).
83. Fedorova, A. D., Tierney, J. A. S., Michel, A. M. & Baranov, P. V. RiboGalaxy: a galaxy-based web platform for ribosome profiling data processing - 2023 update. *J. Mol. Biol.* **435**, 168043 (2023).
84. Bailey, T. L. et al. MEME SUITE: tools for motif discovery and searching. *Nucleic Acids Res.* **37**, W202–W208 (2009).

Acknowledgements

F.Z. is an investigator of SUSTech Institute for Biological Electron Microscopy. The authors acknowledge the assistance of Su Qin in SUSTech Core Research Facilities for performing ultracentrifugation. We thank the SUSTech Core Research Facilities for the supporting of Beckman XPN-100 and Optima MAX-XP. We also thank the cryoEM center at SUSTech for data collection. This work was supported by grants from National Natural Science Foundation of China (Grant No. 32171200 and 92169111 to F.Z.), Shenzhen Science and Technology Program (Grant No. JCYJ20220530115210023 to F.Z.), Guangdong Basic and Applied Basic Research Foundation (Grant No. 2021A1515010805 to F.Z.), Guangdong Innovative and Entrepreneurial Research Team Program (Grant No, 2021ZT09Y104 to F.Z.) and the Guangdong Program (Grant No, 2021QN02Y353 to F.Z.).

Author contributions

T.Y., X.L., and F.Z. designed this study and its experiments. Preparation of cryoEM samples was performed by X.L. and T.Y. CryoEM data were collected by Q.L. and T.Y. Data processing and model building were performed by T.Y. and F.Z. Additional biochemical experiments were performed by X.L., T.Y., W.D., Q.Z., and Z.D. High throughput sequencing data were analyzed by W.D. and F.Z. The results were interpreted by T.Y., X.L., and F.Z. The manuscript was written by T.Y. and F.Z. All authors discussed the results and commented on the manuscript.

Competing interests

The authors declare no competing interests.

Additional information

Supplementary information The online version contains supplementary material available at https://doi.org/10.1038/s41467-025-56797-8.

Correspondence and requests for materials should be addressed to Fuxing Zeng.

Peer review information *Nature Communications* thanks Andrei Korostelev and the other, anonymous, reviewer(s) for their contribution to the peer review of this work. A peer review file is available.